RSC Advances

PAPER

View Article Online
View Journal | View Issue

Cite this: *RSC Adv.*, 2024, **14**, 8752

Synergetic and advanced isotherm investigation for the enhancement influence of zeolitization and β-cyclodextrin hybridization on the retention efficiency of U(VI) ions by diatomite†

Ashour M. Ahmed,*[a] Islam Saad,[b] M. Abdel Rafea[a] and Mostafa R. Abukhadra *[cd]

In synergetic investigations, the adsorption effectiveness of diatomite-based zeolitic structure (ZD) as well as its β-cyclodextrin (CD) hybrids (CD/ZD) towards uranium ions (U(VI)) was evaluated to examine the influence of the transformation procedures. The retention behaviors and mechanistic processes have been demonstrated through analyzing the steric and energetic factors employing the modern equilibrium approach (a monolayer model with a single energy level). After the saturation phase, the uptake characteristics of U(VI) were dramatically improved to 297.5 mg g^{-1} after the CD blending procedure *versus* ZD (262.3 mg g^{-1}) or 127.8 mg g^{-1}. The steric analysis indicated a notable increase in binding site levels after the zeolitization steps (N_m = 85.7 mg g^{-1}) as well as CD implementation (N_m = 91.2 mg g^{-1}). This finding clarifies the reported improvement in the ability of CD/ZD to effectively retain the U(VI) ions. Furthermore, every single active site of the CD/ZD material has the capacity to adsorb around four ions, which are aligned according to a vertical pattern. The energetic aspects, specifically Gaussian energy (<8 kJ mol^{-1}) along with retention energy (<40 kJ mol^{-1}), validate the regulated influences of the physical mechanistic processes. The physical adsorption of U(VI) seems to depend on various intermolecular forces, such as van der Waals forces, in conjunction with zeolitic ion exchanging pathways (0.6–25 kJ mol^{-1}). The thermodynamic assets have been evaluated to confirm the exothermic together with spontaneous adsorption U(VI) by ZD and its blend with CD (CD/ZD).

Received 20th December 2023
Accepted 3rd March 2024

DOI: 10.1039/d3ra08709c

rsc.li/rsc-advances

1 Introduction

Chemical pollution of freshwater sources, together with the ensuing negative consequences on people's wellness and ecological systems, are important challenges that constitute a severe danger to humanity's future prosperity.[1] Toxic wastewater from mining, farming, and factories is constantly being released into the environment without any regulations or controls.[2,3] This is causing the current state of water contamination and the subsequent ecological issues. The potential existence of hazardous metals in aquatic environments, whether in the form of dissolved ions or chemically bonded with other compounds, presents a substantial threat to both the ecological balance and the welfare of people.[2,4] The aforementioned chemicals have been categorized as highly toxic, non-biodegradable, and cancer-causing agents with a propensity to accumulate within the physiological systems of both humans and animals.[4,5] The mining sector, industrial activities, and nuclear fuel processes are substantial contributors of different potentially hazardous and radioactive ions, including uranium, barium, cesium, thorium, and strontium.[6–8]

The nuclear power sector is strongly connected with the generation of a substantial amount of radioactive residues and waste materials.[9–11] Uranium is crucial in the generation of nuclear energy and has been widely established as one of the most radioactive and risky contaminants in water resources.[12,13] Uranium ions have been identified as highly mobile and soluble radioactive ions, particularly in the U(VI) form. This has led to their excessive seepage into water supplies, thereby endangering biological diversity as well as humanity's survival.[14,15] The implementation of uranium(VI) as a contaminant within the food supply to humans results in hepatic injury, renal dysfunction, and eventually mortality. Additionally, the presence of U(VI) pollutants significantly impedes the growth rates of organism embryos, thereby exerting a detrimental impact on the survival as well as reproductive functions of numerous species.[14] To mitigate its detrimental effects, the US

[a]*Physics Department, College of Science, Imam Mohammad Ibn Saud Islamic University (IMSIU), Riyadh 11623, Kingdom of Saudi Arabia*
[b]*Physics Department, Faculty of Science, Beni-Suef University, Beni-Suef, 65211, Egypt*
[c]*Geology Department, Faculty of Science, Beni-Suef University, Beni Suef City, Egypt. E-mail: Abukhadra89@Science.bsu.edu.eg*
[d]*Materials Technologies and Their Applications Lab, Faculty of Science, Beni-Suef University, Beni Suef City, Egypt*

† Electronic supplementary information (ESI) available. See DOI: https://doi.org/10.1039/d3ra08709c

Environmental Protection Agency established the limit levels of U(VI) within drinking water, surface water, and groundwater at 30, 50, and 2000 μg L^{-1}, respectively.[6,16]

The use of new adsorbents for extremely radioactive ion elimination has been described and advocated as a very simple, reusable, and commercially viable technique.[17] The expenses of production, feasibility of manufacturing, recoverable possibility, accessibility, adsorption kinetics, and efficacy of sequestration were all variables considered while assessing the most beneficial structures that may be employed as adsorption agents.[16,18] As a result, comprehensive studies have already been conducted on synthetically produced adsorbents, comprising naturally derived materials, and they have demonstrated remarkable efficacy and potential as adsorbents for the removal of various dissolving toxins.[4,18] Considerable assessments have been conducted on both naturally occurring and synthetic porous silica as well as silicate-based nanoporous materials that have verified effectiveness as adsorbent frameworks owing to their notable surface area, adsorption ability, and profoundly porous characteristics.[19,20] Diatomite refers to a geological scientific term that describes the naturally occurring consolidation formed by the siliceous skeletal structures of diatoms.[21,22] It represents a harmless biomaterial with substantial resources, thermo-chemical stability, surface area, interfacial reactivity, and retention effectiveness.[21,23,24] Consequently, it was widely used in the essential reduction and retention treatments of various species of soluble chemicals within water resources.[21,25] This was assigned to saturation of the diatomite surface with oxygen bridge defects, silicon hydroxyl bridges, and coordination defects, which exhibit remarkable affinities for various kinds of soluble pollutants.[21] Nevertheless, the latest investigation has revealed significant improvements in the morphological and physicochemical characteristics of diatomite through phase and surface-modifying methods.[20,26]

The phase conversion of such natural reactive forms of silica into different species of zeolite, either completely or partially in the form of zeolite/diatomite composite, was suggested in several studies as an effective approach to enhance the technical properties, including surface reactivity, surface area, porous structure, ion exchange capacities, and retention affinities.[27–29] Furthermore, the organic surficial modification or polymeric hybridizing processes, particularly using safe and eco-friendly biopolymers (cellulose, chitosan, and β-cyclodextrin), significantly induce surface reactivity and the abundance of the numerous effective uptake sites on the surface of the silicate structures. This resulted in a promising hybridized adsorbent with enhanced uptake efficiency in addition to its environmental and biodegradable value.[30–33] β-Cyclodextrin (β-CD), an extensively addressed and used oligosaccharide biopolymer, was recommended in several studies to be incorporated as vital components in innovative and effective hybrid adsorbents.[34,35] The previous literature reported several physiochemical advantages for β-CD, including its natural accessibility, chemical stability, biosafety, structural flexibility, and uptake effectiveness.[34,36] Therefore, it was expected that the hybridization of the zeolitic phase of diatomite with β-CD would result in a significant enhancement of the retention efficiency of U(VI) either by providing more active removal sites or by promoting a surficial reactive nature.

Consequently, the current study included a comprehensive examination of three diatomite-based adsorbents to characterize their ability to eliminate U(VI) from aqueous solutions. The three types of adsorbents have been synthesized using the process of phase hydrothermal alteration of diatomite into zeolite, followed by the functioning of the resulting zeolitic phases with β-cyclodextrin by facile dispersion of zeolite within the polymer solutions. These materials comprise untreated diatomite (DI), zeolitic diatomite crystalline phase (ZD), and zeolitic diatomite hybrids with β-cyclodextrin (CD/ZD). The obtained zeolite and CD/ZD displayed enhanced surface area and high saturation of different active chemical groups based on the results of the applied analytic techniques. The investigation focused on examining the effects of various alteration stages upon the adsorption capabilities of the resulting structures, particularly in relation to the interfaces between the adsorbents and U(VI) adsorbate. The objective was attained by employing experimental variables and mathematical aspects derived from modern equilibrium simulation, in accordance with the principles of statistical physics. These parameters declared a significant enhancement in the retention capacity of uranium after the modification process, which was correlated with the enhancement in the surface area and the quantities of the active chemical groups.

2 Experimental sections

2.1 Materials

Processed naturally formed diatomite (97.87% purity) has been acquired from Egypt's Central Metallurgical and Development Institute. The starting sample underwent chemical refinement through acid-washing protocols utilizing hydrochloric acid (37% pure) along with hydrogen peroxide (30% pure) to get rid of calcareous, organic, and metal-based substances (Cornel Lab Company; Egypt). Aluminum hydroxide $(AlOH)_3$ and sodium hydroxide (NaOH) pellets with a grade of 97% were obtained from Sigma-Aldrich in Egypt and utilized in the zeolitization processes of diatomite powder. For the simple modification of zeolitized diatomite, commercial β-cyclodextrin as a crystalline polymer (>85% purity) along with pure ethanol (95% purity) was employed.

2.2 Fabrication of zeolite from diatomite (ZD)

4 g of diatomite had been subjected to an acidic cleaning phase for a duration of 4 hours utilizing a diluted hydrochloric acid solution (10%). Afterwards, a rinsing step employing H_2O_2 was carried out to guarantee the thorough elimination of any impurities connected with the precursor material. The refined material was employed in the alkaline hydrothermal process of zeolitization. The diatomite as powder had been blended with $Al(OH)_3$ throughout a solution of NaOH, having a volume of 100 mL. The mixture was stirred using an electromagnetic stirrer for 120 minutes at a precisely controlled 1000 rpm speed and a temperature of operation of around 50 °C. The blend was

prepared by mixing all of the chemicals at specific molar ratios (Si/Al (1/1.3), Na_2O/SiO_2 (1.4/1), and H_2O/Na_2O (40/1)). Subsequently, the mixes were meticulously poured into an autoclave lined with Teflon with a volume of 150 mL, serving as the transformation system. The autoclave was then subjected to thermal treatment at a temperature of 120 °C for a duration of 5 hours. Subsequently, synthesized zeolitized diatomite particulates have been separated out of the residual alkaline solution, subjected to a washing process, and neutralized using distilled water. Lastly, the resulting particles had been dried for 12 hours at a temperature of 85 °C.

2.3 Production β-cyclodextrin/zeolitic diatomite composite (CD/ZD)

The procedure for functionalizing ZD particulates using β-cyclodextrin was carried out employing the approach described by Altoom *et al.*,.[31] The CD powder (1 g) had initially been dispersed and pulverized into roughly 80 mL of ethanol throughout the duration of 3 hours utilizing a magnetic stirrer set at 1000 rpm, resulting in the formation of a slurry-like mixture. In the context of a collaborative test, the earlier synthesized ZD particulates, weighing 2 g, had been subjected to dispersion and homogenization for a duration of 60 minutes. This process was carried out by swirling the particulates into 100 mL of distillate water at a speed of 1000 rpm while simultaneously applying a sonication generator with a power output of 240 W. Subsequently, the ZD mixture and the slurry-like solution of CD were added together and subjected to homogenization *via* stirring processes at a speed of 1000 rpm for a duration of 24 hours. Afterwards, a further blending process was conducted for a duration of 24 hours *via* a sonication generator with a power output of 240 W. The resulting composite particulates were further separated from the residual solution through the use of a Whatman filter paper. The recovered material underwent a washing process using distilled water to purify and neutralize the outermost layer of CD/ZD. After that, it underwent drying at a temperature of 60 °C for a duration of 12 hours.

2.4 Characterization techniques

The levels of crystallization and phase detection of crystalline structures were assessed using a PANalytical-Empyrean X-ray diffractometer. This instrument has a measurement range spanning from 0 to 70°. The structural groups of DI, ZD, and CD/ZD, in comparison with kaolinite, were identified using a Fourier transform infrared spectrometer (FTIR8400S; Shimadzu) with a detection wavelength range of 400 to 4000 cm^{-1}. The morphologies of DI, ZD, and CD/ZD and their changes according to the kaolinite base morphology were examined during various transformation steps through the analysis of SEM photos. The photographs were captured using the scanning electron microscope (Gemini, Zeiss-Ultra 55) subsequent to the application of thin layers of gold throughout the exteriors of DI, ZD, and CD/ZD. The porosity and surface area of DI, ZD, and CD/ZD were ascertained by examining the corresponding N_2 adsorption and desorption isotherms employing a surface area analyzer (Beckman Coulter SA3100).

2.5 Adsorption studies

Adsorption strategies for eliminating uranium ions (U(VI)) were tested in batches utilizing DI, ZD, and CD/ZD. The investigation employed standard experimental variables, such as pH levels that ranged from 2 to 8, retention periods spanning from 30 to 880 minutes, and U(VI) concentrations between 50 until 350 mg L^{-1}. Furthermore, the experimental conditions included the manipulation of the evaluating temperature, which was systematically changed throughout a range spanning from 293 K to 313 K. In addition, the remaining key testing factors were deliberately selected and consistently retained at predetermined values across the duration of the study [the volume was set at 200 mL and the amount of solid dose at 0.2 g L^{-1}]. The design of the experiments has been analyzed in three separate experiments, utilizing the mean values for all determined concentrations in addition to the resultant estimations or observations. After the equilibrium stage, the solid particulates of DI, ZD, and CD/ZD were taken away from the U(VI) solutions using Whatman filter paper. The level of U(VI) in the analyzed solutions has been measured by applying inductively coupled plasma mass spectrometry (ICP-MS) equipment that is supplied by PerkinElmer. The U(VI) standard utilized throughout measurements had been subject to verification by the National Standard & Technology Institute (NIST), while the reference standard was purchased *via* Merck Company (Germany). The determination of the adsorption capacities (Q_e) of U(VI) by DI, ZD, and CD/ZD was estimated in mg g^{-1} employing eqn (1). The computation considered various factors, including the volume (V), the dosages of DI, ZD, and CD/ZD (m), the initial concentration of U(VI) (C_o), and the final concentration of U(VI) (C_e).[2]

$$Q_e(\text{mg g}^{-1}) = \frac{(C_o - C_e)V}{m} \quad (1)$$

2.6 Equilibrium studies

The adsorption tests were modelled using various modelling techniques, including standard kinetic, common isotherm, and advanced equilibrium models. The advanced or modern models were developed based on hypotheses developed from the fundamentals of statistical physics (Table S1†). Nonlinear regression methodologies were employed to conduct kinetic and traditional equilibrium analyses. The analysis took into account the numerical formulas of the previously implied models. The correlation coefficients (R^2) (eqn (2)) and chi-squared (χ^2) (eqn (3)) values are the most important signs of how well the model fits the data. The evaluation of the consistency between the uptake activities' matching levels and the modern models was achieved through the utilization of the coefficient of correlation (R^2) in conjunction with the root mean square error (RMSE), as indicated by eqn (4). The symbols m', p, Qi_{cal}, and Qi_{exp} represent the empirical data obtained, the

variables investigated, the predicted U(VI) adsorption, and the confirmed U(VI) adsorption capacity, respectively.[2]

$$R^2 = 1 - \frac{\sum\left(q_{e,exp} - q_{e,cal}\right)^2}{\sum\left(q_{e,exp} - q_{e,mean}\right)^2} \quad (2)$$

$$\chi^2 = \sum \frac{\left(q_{e,exp} - q_{e,cal}\right)^2}{q_{e,cal}} \quad (3)$$

$$\mathrm{RMSE} = \sqrt{\frac{\sum_{i=1}^{m}\left(Qi_{cal} - Qi_{exp}\right)^2}{m' - p}} \quad (4)$$

3 Results and discussion

3.1 Characterization

The X-ray diffraction (XRD) patterns acquired were utilized to track the progression of both the phase transition and the functioning procedures. The diatomite powder frustules that have been used show a unique pattern that can tell the difference between opaline and amorphous silica. This pattern includes a large, noticeable peak seen at a 2 theta position of 22° (Fig. 1A). The zeolitic phases that were obtained for diatomite (ZD) demonstrate a notable transformation of the siliceous composition of diatomite to well-crystalline synthesized zeolite phases, including synthesized sodalite (JCPDS # 01-071-53569) and zeolite Na-A (ICCD ref. code no. 00-039-0222) (Fig. 1B). Regarding the pattern of β-cyclodextrin in its distinct phase, it reveals its highly crystallized form based on the detectable distinct diffraction peaks (6.80°, 10.83°, 12.57°, 12.64°, 13.0°, 15.55°, 18.90°, 19.80°, 23.00°, 25.81°, 30.30°, and 34.90°) (Fig. 1C). The established pattern of the generated CD/ZD hybrid confirms the successful blending of the zeolite phases as a base with the polymeric structure (Fig. 1D). The pattern provides evidence for the presence of identifying peaks corresponding to the zeolite phases, specifically the sodalite phase and well-synthesised zeolite-A (Fig. 1D). Additionally, the distinctive peaks of the CD are also observed. Nevertheless, the identified peaks exhibited substantial deviations from their initial placements, along with a significant drop in their magnitudes. The aforementioned findings confirm the substantial incorporation and reactions that occur between the reactive functional groups of the zeolitic phases and the chemical structure of the polymer.

The analysis of alterations in the essential chemical groups during the different synthesizing procedures was assessed considering the determined FT-IR spectra. The spectrum of DI demonstrates clearly that the known chemical groups of non-crystalline silica include Si–O (at a wavelength of 465 cm^{-1}), asymmetrical Si–O–Si (at 700 cm^{-1}), symmetrical Si–O–Si (at 1092.1 cm^{-1}), H–O–H (at 1638.13 cm^{-1}), and Si–O–H (at 3437 cm^{-1}) (Fig. 2A).[20,25] The spectrum of ZD demonstrates the successful transformation of the diatomite siliceous composition into crystallite phases of zeolite (sodalite and zeolite-A) (Fig. 2B). The main zeolitic chemical groups were detected clearly, including Si–OH (3610 cm^{-1}) and Al–OH (3427 cm^{-1}) groups in addition to the coordinated water inside the internal channels of zeolite (1471 cm^{-1}), bending of Si–O–Si (992 cm^{-1}), Si–O group (708 and 454 cm^{-1}), and Si–O–Al group (636 and 551 cm^{-1}) (Fig. 2B).[37]

The organic chemical groups of β-cyclodextrin (polysaccharides and glycosidic) as a pure phase were identified significantly from its spectrum. These groups involve O–H at 3376 cm^{-1}, –CH/CH_2 asymmetrical stretching at 2926 cm^{-1}, O–H bending at 1636 cm^{-1}, C–O–C stretching at 1200 cm^{-1}, H–O–H deformation in the CD cavity at 1666.2 cm^{-1}, C–O stretching at 1000 cm^{-1}, C–OH bending vibration at 1482 cm^{-1}, and asymmetric glycosidic C–O–C stretching at 1158 cm^{-1} (Fig. 2C).[38,39] The FT-IR spectra of CD/ZD demonstrated the efficient hybridization of the zeolitic phases from diatomite by the main chemical functionalities of CD (Fig. 2D). The main

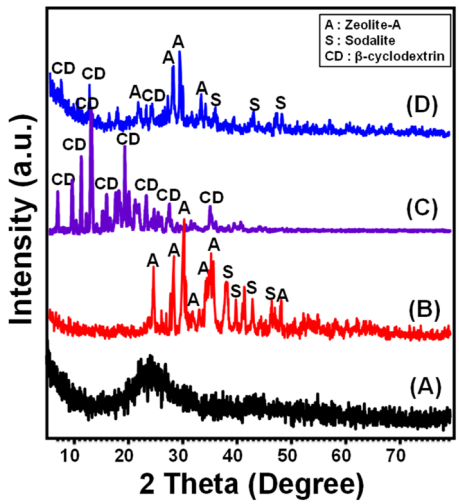

Fig. 1 XRD pattern of starting diatomite (A), zeolitic diatomite (B), integrated CD polymer (C), and the prepared CD/ZD composite (D).

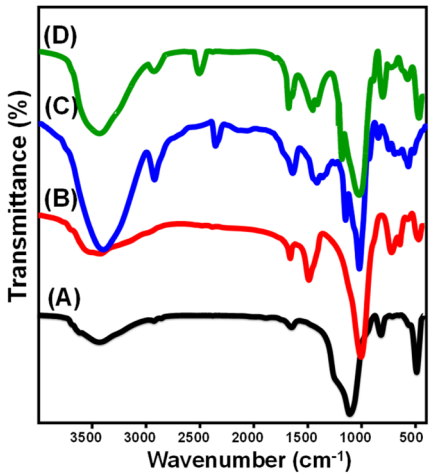

Fig. 2 FT-IR spectra of starting diatomite (A), zeolitic diatomite (B), integrated CD polymer (C), and the prepared CD/ZD composite (D).

groups of zeolite (Si–O (around 450 cm^{-1}), asymmetrical Si–O–Si (around 710 cm^{-1}), coordinated water (around 1427 cm^{-1}), symmetrical Si–O–Si (around 1008 cm^{-1}), and Si–O–H (around 3435 cm^{-1})) and those of CD (–CH/CH_2 (around 2918 cm^{-1}), C–OH bending (around 1474 cm^{-1}), and C–O–C (around 1214 cm^{-1})) in the same pattern confirms the successful hybridization between them (Fig. 2D). The previous results are in agreement with the EDX analysis (Fig. S1†).

The evaluation of morphological findings pertaining to the modification techniques was conducted based on the analysis of SEM images (Fig. 3). The unprocessed diatomite displays the distinctive geometries of the siliceous frustules or skeletal properties of diatoms (Fig. 3A). The inspected grains displayed a high degree of porosity and had a pinnate-like structure. The SEM images of ZD demonstrate the successful transformation of diatomite into two distinct zeolitic phases (zeolite-A and sodalite) exhibiting various morphologies (Fig. 3B and C). The sodalite phase exhibits a highly formed and visually striking floral structure, whereas synthesized zeolite-A possesses its own unique cubic geometry (Fig. 3C). Furthermore, the zeolitic crystals exhibit an irregular distribution pattern and adhere to the outside of the pinnate structure of diatomite, closely mimicking its shape. Notably, the presence of undamaged remnants of the diatom frustules was detected. This provides support for the incomplete and limited transformation of the involved diatomite portions into zeolite, indicating the potential development of a hybrid framework consisting of synthesized zeolite and diatomite. Following blending processes of CD polymeric, the SEM images of CD/ZD exhibit the reoriented state of the zeolitic crystals within newly formed aggregated particles related to the matrix of the polymer possessing totally different morphology and rough topography (Fig. 3D–F). The polymeric matrix exhibited distinct worm-like or lenticular-shaped granules, ranging in size between 100 and 500 nm (Fig. 3F). Additionally, the magnified photos declare the ornamentation of these particles with nano-dots or nano-spheres, which increase the overall surface area of the resulting structure (Fig. 3D and E). The key texture characteristics as a result of the two modification steps were assessed based on the surface area. The unprocessed diatomite has a remarkable surface area of 117.7 $m^2\ g^{-1}$, which was enhanced to 356 $m^2\ g^{-1}$ after the zeolitization reactions and up to 364.3 $m^2\ g^{-1}$ after the modification process with CD. This increase can be attributed to the composite's morphologies, as described earlier.

3.2 Adsorption studies

3.2.1 Effect of pH. The influence of pH values spanning 2 to 8 on the quantity of U(VI) to be adsorbed was examined employing DI, ZD, and CD/ZD as highly efficient adsorbents. The aforementioned laboratory tests were conducted with careful control over key factors such as the level of U(VI) of 100 mg L^{-1}, a time frame of 120 minutes, a solid dosage of 0.2 g L^{-1}, a volume of 200 mL, and a temperature of 20 °C. These factors were scrupulously maintained at their assigned levels throughout the experiments. The retention efficiencies of U(VI) determined by using DI, ZD, and CD/ZD show considerable improvements as the pH of the polluted solutions being studied increases from pH 2 (12.5 mg g^{-1} (DI), 18.7 mg g^{-1} (ZD), and 23.5 mg g^{-1} (CD/ZD)) until pH 5 (66.5 mg g^{-1} (DI), 77.8 mg g^{-1} (ZD), and 95.4 mg g^{-1} (CD/ZD)) (Fig. 4). Subsequently, the noticed rise in pH triggered a substantial reduction in the confirmed retention efficiencies of U(VI) by both DI and its synthesized adsorbents. Nevertheless, this retention

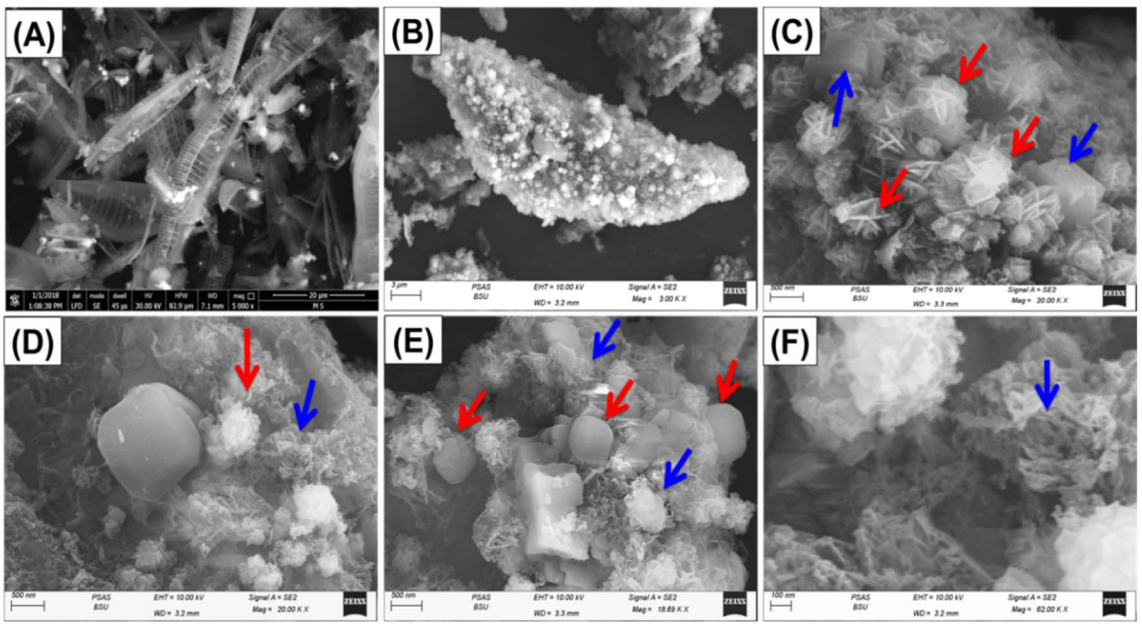

Fig. 3 SEM images of starting diatomite (A), zeolitic diatomite (B), high magnification on the formed zeolite phases (red arrows refer to sodalite and blue arrows refer to zeolite-A) (C), synthetic CD/ZD composite (zeolite (red arrows) and polymeric matrix (blue arrows)) (D and E), high magnification images on the integrated polymeric matrix of CD (F).

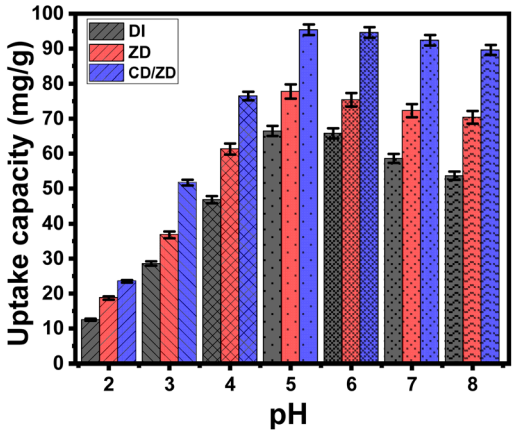

Fig. 4 The influence of the pH values on the retention of U(VI) ions by DI, ZD, and CD/ZD.

effectiveness remained significant until a pH of 8. Therefore, such materials have the potential to be used as effective adsorbents in actual purification operations, aligning with a pH level of 6 to 9 recommended by the US Environmental Protection Agency (EPA) for the treatment of industrial effluents.[40] The presented behaviors demonstrate a significant association between the pH and the ionization properties of U(VI) ions, alongside the electrical charges across the exteriors of DI, ZD, and CD/ZD.[6] Uranium(VI) mostly exists in a monomeric state as UO_2^{2+} and in smaller quantities as $UO_2(OH)^+$ at pH levels equal to or less than 4.3. Beyond pH 5, U(VI) is found in either colloidal or oligomeric phases such as $(UO_2)_2(OH)_2^{2+}$, $(UO_2)_4(OH)_7^+$, and $(UO_2)_3(OH)_5^+$, $UO_2(OH)_3^-$, and $(UO_2)_3(OH)_7^-$, with dominant existence for the negative species at the alkaline conditions.[6,41]

Consequently, the attraction of its ions at low pH levels led to a significant degree of competitiveness and repulsive responses involving the H^+ (or H_3O^+) and UO_2^{2+} on the binding sites of DI, ZD, and CD/ZD. This phenomenon exhibited a steady decline in its impact until reaching a pH of 5. When the pH exceeds 5, the surfaces of DI as well as ZD and CD/ZD acquire a greater quantity of negative charges, which causes notable repulsive behaviors with the existing negative U(VI) species.[11,39,42] The DI, ZD, and CD/ZD surfaces exhibited negative charges attributed to the abundance of hydroxyl groups across their outermost surfaces. At low pH levels, the presence of H^+ ions reduces the negative impedance of their surfaces, therefore hindering the uptake of positively charged U(VI) ions. Thus, it is clear from the plot in Fig. 4 that the external electronegativity of DI, ZD, and CD/ZD has the greatest impact in slightly acidic and barely alkaline environments. In these conditions, the electrostatic attraction influence is enhanced, resulting in an elevated overall retention rate compared to the highly acidic environment. As a result, the optimal pH value of DI, ZD, and CD/ZD for U(VI) retention was 5, and this value was employed in further studies.

3.2.2 Effect of contact time. An investigation was conducted to examine the influence of the duration of U(VI) retention on the practically determined capacities of DI, ZD, and CD/ZD throughout a time interval that extends from 30 to 880 minutes. This was achieved following the adjustment of additional significant variables to predetermined values [U(VI) concentration: 100 mg L^{-1}; pH: 5; volumes: 200 mL; temperature: 20 °C; solid material dosage: 0.2 g L^{-1}]. The efficacy of DI, ZD, and CD/ZD in the adsorption of U(VI) displays notable enhancement in measured elimination rates as well as the estimated quantities of retained U(VI) in mg g^{-1}. Furthermore, it is worth noting that the duration of the tests exerts a regulatory influence on the aforementioned observed increments (Fig. 5A). The rising impact of U(VI) retaining activities using DI, ZD, and CD/ZD can be easily detected for a period of up to 420 minutes. Following the designated duration of contact, there were no observable variations or enhancements in the rates of U(VI) retention or the quantities of U(VI) trapped. This observation indicates that the system maintained a state of stability after 420 minutes, which was defined as the point of adsorption equilibrium (Fig. 5A). The U(VI) equilibrium retaining levels of the DI, ZD, and CD/ZD were determined to be 102.6 mg g^{-1} (DI), 124.5 mg g^{-1} (ZD), and 141.3 mg g^{-1} (CD/ZD) (Fig. 5A). The preliminary phases of the accomplished tests revealed that the existence of a substantial number of unbound and chemically active groups or retaining receptors situated across the structures of DI, ZD, and CD/ZD resulted in significant enhancements with respect to the rate of U(VI) elimination and the quantities of U(VI) retained.[34] The prolonged time frame of examinations results in a considerable diminution in the availability of these vacant receptors due to the longer-term retention of U(VI) and subsequent occupancy and reduction of these receptors. As a result, during a specified duration, the rates at which U(VI) was adsorbed encountered a notable decrease, whereas the retention properties of DI, ZD, and CD/ZD remained unchanged or exhibited negligible improvement. Once all the receptors or available reaction sites are fully occupied by U(VI), the equilibrium states of DI, ZD, and CD/ZD are developed.[2]

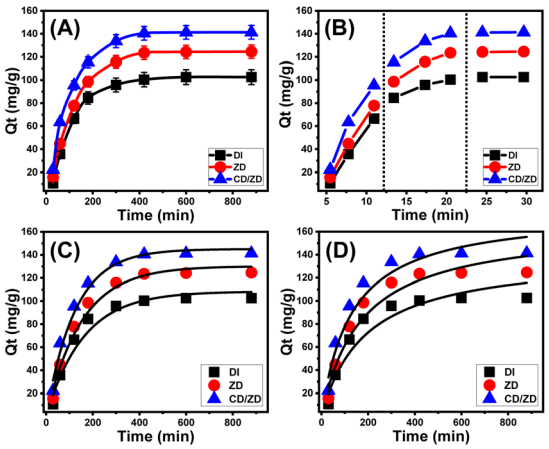

Fig. 5 The influence of contact time on the retention of U(VI) by DI, ZD, and CD/ZD (A), the intra-particle diffusion curves (B), pseudo-first order kinetic model fitting results (C), and pseudo-second order kinetic model fitting results (D).

3.2.3 Intra-particle diffusion behavior. The uptake activities of U(VI) using DI, ZD, and CD/ZD can be assessed by analyzing the intra-particle diffusion curves. These curves display three discrete segments that have various slopes. The curves spotted in the current study do not display any evident crossings with their starting points, suggesting the coexistence of multiple adsorption mechanisms alongside U(VI) diffusion pathways.[6,43] The operational procedures may involve the subsequent essential stages: The process involves the binding of U(VI) to receptors located on the exteriors of DI, ZD, and CD/ZD (boundary). Additionally, intra-particle diffusion and the mechanism of reaction, which includes phases of saturating and stabilizing states, are also factors in this process.[44] The preliminary findings of this study suggest that the primary mechanisms involved in the retention of U(VI) onto the external surface of DI, ZD, and CD/ZD comprised the most influential mechanistic pathways throughout the experiment's course (Fig. 5B). The efficacy of the U(VI) retained reactions during this phase relies on the collective quantities of available receptors along the surfaces of DI, ZD, and CD/ZD.[45] The identification of recently formed phases was enhanced by prolonging the period, showcasing the effectiveness of many additional processes known as layered adsorption techniques (Fig. 5B).[3,44] Furthermore, these supplementary procedures also incorporate the effects of U(VI) diffusion activities. In the end, it was established that the final three stages demonstrate a significant presence whenever DI, ZD, and CD/ZD accomplish states of balance with U(VI) adsorption. This observation suggests the quantity of U(VI) ions that have been efficiently retained has completely filled the binding sites that are accessible.[4,6] The elimination of uranium is subject to molecular interactions together with interionic attraction processes during these stages of the retention course.[39]

3.2.4 Kinetic modeling. The kinetic properties of U(VI) elimination processes *via* DI, ZD, and CD/ZD have been discussed using the standard kinetic concepts of pseudo-first order (P.F.) and pseudo-second order (P.S.) numerical models. The level of agreement between the U(VI) retaining processes and the kinetic theories has been denoted by the corresponding formulas and determined by both the R^2 value (correlation coefficient) and the chi-squared (χ^2) statistics (Table 1; Fig. 5C and D). The obtained values of R^2, along with χ^2, suggest that the kinetic properties and principles of the P.F. model provide a more suitable fit for the uptake behaviors of U(VI) *via* DI, ZD, and CD/ZD in comparison to the assessed P.S. model. The results gathered through the tests that were performed with DI, ZD, and CD/ZD under conditions of equilibrium (102.6 mg g^{-1} (DI), 124.5 mg g^{-1} (ZD), and 141.3 mg g^{-1} (CD/ZD)) proved very consistent with the results derived from mathematical calculations computed using the model (108.3 mg g^{-1} (DI), 130.1 mg g^{-1} (ZD), and 145 mg g^{-1} (CD/ZD)). This consistency affords additional support for the previous findings highlighted during the kinetic analysis (Table 1). According to the basic concepts of the P.F. theory, it is implied that the main influences impacting the capture of U(VI) through DI, ZD, and CD/ZD are physical mechanisms, such as van der Waals forces together with electrostatic attraction.[46–48]

Table 1 The mathematical parameters of the studied kinetic models

Material	Model	Parameters	Values
DI	Pseudo-first-order	K_1 (min^{-1})	0.0062
		$Q_{e\ (cal)}$ (mg g^{-1})	108.3
		R^2	0.96
		χ^2	1.56
	Pseudo-second-order	k_2 (mg g^{-1} min^{-1})	3.83×10^{-5}
		$Q_{e\ (cal)}$ (mg g^{-1})	140
		R^2	0.94
		χ^2	2.53
ZD	Pseudo-first-order	K_1 (min^{-1})	0.0066
		$Q_{e\ (cal)}$ (mg g^{-1})	130.1
		R^2	0.97
		χ^2	0.94
	Pseudo-second-order	k_2 (mg g^{-1} min^{-1})	3.56×10^{-5}
		$Q_{e\ (cal)}$ (mg g^{-1})	165.4
		R^2	0.95
		χ^2	1.9
CD/ZD	Pseudo-first-order	K_1 (min^{-1})	0.008
		$Q_{e\ (cal)}$ (mg g^{-1})	145
		R^2	0.98
		χ^2	0.85
	Pseudo-second-order	k_2 (mg g^{-1} min^{-1})	4.33×10^{-5}
		$Q_{e\ (cal)}$ (mg g^{-1})	178.2
		R^2	0.95
		χ^2	1.82

3.2.5 Effect of U(VI) concentrations. The influence of starting U(VI) concentrations has been analyzed in order to determine the best capacities of DI, ZD, CD/ZD, and their respective states of equilibrium within the practically assessed ranges of 50 to 350 mg L^{-1}. The other retention factors have been adjusted to be at specified levels [dosage: 0.2 g L^{-1}; contact period: 24 hours; water volume: 200 mL; pH: 5; temperature: ranging from 293 K to 313 K]. The concentrations of U(VI) displayed a significant increase in the total quantities of U(VI) retained by DI, ZD, and CD/ZD (Fig. 6). The increased concentrations of U(VI) ions within a given volume led to a noticeable improvement in their diffusion, transport, propagation, and driving forces, thereby promoting interactions and collisions with a greater number of accessible and functional receptors that are located outside of ZD, CD/ZD, and DI. As a result, the performance of the U(VI) retaining processes conducted by DI, ZD, and CD/ZD was significantly improved.[31] The observed levels of U(VI) elimination demonstrate a positive correlation with the starting concentration, up to specific thresholds. Following this, an increase in the starting concentration of U(VI) does not seem to have any discernible impact on the amount of ions that were retained on DI, ZD, and CD/ZD (Fig. 6A, B, and C). This differentiation in their equilibrium stages assists in identifying the exact maximal potential for U(VI) retention. The adsorption values under equilibrium situations of DI are 188.4 mg g^{-1} at 293 K, 163.6 mg g^{-1} at 308 K, and 135.8 mg g^{-1} at 313 K (Fig. 6A). The experimental results indicate that the equilibrium capacities of ZD are as follows: 252.8 mg g^{-1} at 293 K, 215.4 mg g^{-1} at 308 K, and 175.5 mg g^{-1} at 313 K (Fig. 6B). In

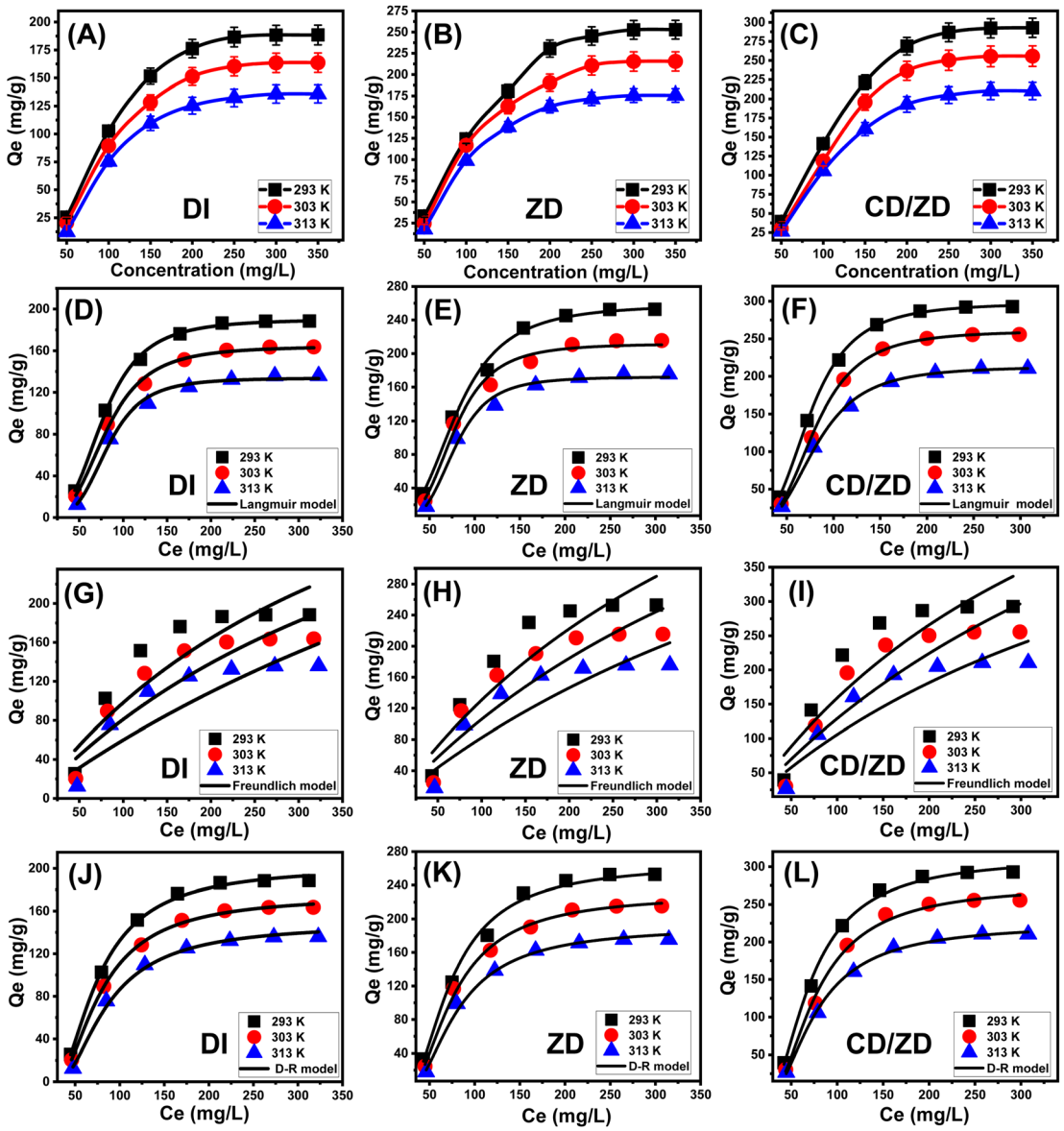

Fig. 6 The influence of initial U(VI) concentrations on the determined retention capacities (DI (A), ZD (B), and CD/ZD (C)), fitting of the U(VI) retention processes with conventional Langmuir model (DI (D), ZD (E), and CD/ZD (F)), fitting of the U(VI) retention processes with conventional Freundlich model (DI (G), ZD (H), and CD/ZD (I)), and fitting of the U(VI) retention processes with conventional D–R model (DI (J), ZD (K), and CD/ZD (L)).

the presence of CD/ZD, the equilibrium concentrations of U(VI) are linked to adsorption capacities of 292.8 mg g^{-1} at 293 K, 255.7 mg g^{-1} at 308 K, and 210.3 mg g^{-1} at 313 K (Fig. 6C). The enhanced retention properties of CD/ZD over DI and ZD may be a result of two reasons: (1) the expanded surface area and (2) the notable increase in the total number of active sites following the integration of CD polymers. The better characteristics of ZD in comparison to DI can potentially be attributed to the notable enhancements in fundamental ion exchange mechanisms, surface reactive properties, and surface area obtained through zeolitization strategies. The noticeable decrease in the retention of U(VI) *via* DI, ZD, and CD/ZD as a function of the experiment's temperature indicated the exothermic characteristics of the processes that occurred.

3.2.6 Giles's classification. The isotherm curves for the U(VI) employing DI, ZD, and CD/ZD had been categorized based on the specifications set out by Giles' classification. The analysis revealed that the observed curves demonstrated L-type equilibrium (Fig. 6A–C). The equilibrium properties of the L-type isotherm demonstrate the significant impacts arising from intermolecular attractive interactions that occur throughout the adsorption mechanisms of U(VI) by DI, ZD, and CD/ZD. The aforementioned impacts are also intensified by the robust interactions that exist between U(VI) ions and the reactive chemical structures of DI, ZD, and CD/ZD.[49] According to the

criteria of the L-type isotherm, it was feasible to predict the formation of complete monolayers of sequestrated U(VI) over the outer surfaces of DI, ZD, and CD/ZD particles.[50] Furthermore, the detectable isothermal style suggests the DI, ZD, and CD/ZD particulates are characterized by diverse and substantial functioning and free uptake receptors. These receptors exhibit notable selectivity for the U(VI) ions throughout all phases of the adsorption process, particularly in cases where the starting concentrations were low.

3.2.7 Classic isotherm models. The present investigation analyzes the adsorption behavior of U(VI) on DI, ZD, and CD/ZD particulates, applying the Langmuir, Freundlich, and Dubinin–Radushkevich (D–R) isotherm models to establish the equilibrium aspects of U(VI) retention. The findings derived from the examination of R^2 and χ^2 demonstrate that the U(VI) retention behaviors shown by DI, ZD, and CD/ZD particulates are more consistent with the principles of the Langmuir isotherm theory in comparison to the base assumptions of the Freundlich theory (Table 2; Fig. 6D–L). The Langmuir isotherm principle elucidates the homogeneous adsorption behavior of U(VI) ions onto the vacant and active binding positions of DI, ZD, and CD/ZD particulates in a monolayer arrangement.[46,47] According to theoretical calculations, the greatest possible adsorption capacities (Q_{max}) of U(VI) by DI at various temperatures are 190.2 mg g^{-1} (293 K), 164.2 mg g^{-1} (303 K), and 137.7 mg g^{-1} (313 K).

The calculated values obtained utilizing the ZD are 258.6 mg g^{-1} at a temperature of 293 K, 219.8 mg g^{-1} at 308 K, and 178.3 mg g^{-1} at 313 K. The predicted maximum capacities by CD/ZD at various temperatures are: 297.7 mg g^{-1} at 293 K, 260.8 mg g^{-1} at 303 K, and 213.2 mg g^{-1} at 313 K (Table 2).

The D–R model's equilibrium principles (Fig. 6J–L) and Gaussian energy (E) derived *via* the D–R equation are of utmost importance in distinguishing the mechanistic pathways (chemical or physical) involved in the capture of U(VI).[51] The values computed for the E parameter pertaining to U(VI) retention behaviors by DI, ZD, and CD/ZD correspond to the assumed energies suggested for cooperation mechanisms underlying

Table 2 The mathematical characteristics of the traditional isotherm models under consideration

			293 K	303 K	313 K
DI	Langmuir model	Q_{max} (mg g^{-1})	190.2	164.2	137.7
		b (L mg^{-1})	3.7×10^{-7}	3.24×10^{-7}	1.51×10^{-8}
		R^2	0.99	0.99	0.99
		χ^2	0.05	0.13	0.17
	Freundlich model	$1/n$	0.80	0.84	0.94
		k_F (mg g^{-1})	2.27	1.61	1.24
		R^2	0.82	0.85	0.83
		χ^2	4.92	3.17	3.59
	D–R model	β (mol^2 kJ^{-2})	0.041	0.046	0.056
		Q_m (mg g^{-1})	201.7	174.3	147.9
		R^2	0.999	0.99	0.99
		χ^2	0.05	0.028	0.17
		E (kJ mol^{-1})	3.49	3.29	2.98
ZD	Langmuir model	Q_{max} (mg g^{-1})	258.6	219.8	178.3
		b (L mg^{-1})	2.8×10^{-6}	1.43×10^{-7}	2.03×10^{-8}
		R^2	0.99	0.99	0.99
		χ^2	0.35	0.71	0.38
	Freundlich model	$1/n$	0.83	0.87	0.90
		k_F (mg g^{-1})	2.67	1.84	1.2
		R^2	0.86	0.84	0.82
		χ^2	4.43	5.71	6.99
	D–R model	β (mol^2 kJ^{-2})	0.016	0.021	0.032
		Q_m (mg g^{-1})	265.6	229.3	190.6
		R^2	0.99	0.99	0.99
		χ^2	0.33	0.21	0.29
		E (kJ mol^{-1})	5.6	4.9	3.95
CD/ZD	Langmuir model	Q_{max} (mg g^{-1})	297.7	260.8	213.2
		b (L mg^{-1})	7.7×10^{-7}	3.4×10^{-7}	6.1×10^{-7}
		R^2	0.99	0.99	0.99
		χ^2	0.029	0.011	0.067
	Freundlich model	$1/n$	0.81	0.87	0.84
		k_F (mg g^{-1})	3.53	2.21	2.03
		R^2	0.84	0.85	0.86
		χ^2	6.12	5.24	5.02
	D–R model	β (mol^2 kJ^{-2})	0.0081	0.0088	0.011
		Q_m (mg g^{-1})	312.5	275.9	223.6
		R^2	0.99	0.99	0.99
		χ^2	0.19	0.31	0.087
		E (kJ mol^{-1})	7.85	7.5	6.7

weak chemical and physical reactions (8 to 16 kJ mol^{-1}). Furthermore, it should be noted that the aforementioned levels fall inside the zeolitic ionic exchange mechanisms' designated limits, which typically range from 0.6 to 25 kJ mol^{-1}.[6]

3.2.8 Advanced isotherm modeling. The most recent advancements in equilibrium simulations, which rely on statistical physics hypotheses, may offer substantial insights into the distinctive features of adsorption operations, specifically concerning the interfaces that exist between the contaminants and the exterior features of heterogeneous solid adsorbent. The statistical properties gained from these mathematical models, including energy and steric considerations, have the potential to provide insights into the underlying mechanism. The steric aspects encompassed three primary parameters: the quantity of U(VI) ions present at each site ($n_{(U(VI))}$), the total quantity of sites occupied by U(VI) on the DI, ZD, and CD/ZD interfaces ($N_{m\ (U(VI))}$), as well as the maximum capacity of DI, ZD, and CD/ZD to adsorb U(VI) at full saturation ($Q_{sat\ (U(VI))}$). The factors associated with energetic aspects encompassed internal energy (E_{int}), free enthalpy (G), entropy (S_a), and U(VI) removal energy (E). The evaluation of the statistical model for analyzing the retention activities of U(VI) involved the use of non-linear fits using the representative equations pertaining to these models. The investigation described above was successfully completed by employing multivariable nonlinear regression modeling in combination with the Levenberg–Marquardt iterative process. The fitness levels noticed were utilized to investigate and elucidate the adsorption approaches for U(VI) by DI, ZD, and CD/ZD using a monolayer model with a single energetic site. The analysis is presented in Table 3 and Fig. 7A–C.

3.2.9 Steric properties

3.2.9.1 Number of adsorbed U(VI) ions ($n_{(U(VI))}$) per each site. The $n_{(U(VI))}$ factor computed significantly indicates the orientation (horizontal or vertical) of the uranium ions that were retained on the exteriors of DI, ZD, and CD/ZD. These findings have more implications for the determination of the underlying mechanistic processes, particularly the differentiation between multi-docking and multi-ionic. In systems subjected to multiple anchoring or docking activities, several sites of adsorption exhibit horizontal arrangements occupied by a single U(VI) ion. A single receptor site can attract numerous U(VI) ions in non-parallel, beside a vertical arrangement for the mechanisms having values greater than one. Multi-ionic mechanistic activities are the primary cause of such retention characteristics.[4,52] The calculated values of $n_{(U(VI))}$ for DI ($n_{(U(VI))}$ = 3.4–4.08), ZD ($n_{(U(VI))}$ = 3.06–4.07), and CD/ZD ($n_{(U(VI))}$ = 3.25–3.39) all exceed 1 (Table 3; Fig. 7D). Since each absorbing site of DI and ZD was capable of accepting up to five ions of U(VI) and four ions for CD/ZD, which were dispersed in non-parallel vertical positions by multi-ionic processes.

The estimated $n_{(U(VI))}$ values similarly show considerable behavioral changes with regard to temperature impacts. For DI, the values provided of $n_{(U(VI))}$ with respect to temperature indicate minor variations, with the value decreasing by ascending from 293 K ($n_{(U(VI))}$ = 3.4) to 308 K ($n_{(U(VI))}$ = 3.3) and then increasing by rising to 313 K ($n_{(U(VI))}$ = 4.08) (Table 3; Fig. 7D). For CD/ZD, the trend was inverted as the value rose alongside the temperature from 293 K ($n_{(U(VI))}$ = 3.26) until 308 K ($n_{(U(VI))}$ = 3.39); afterwards, it fell immediately when the temperature reached 313 K ($n_{(U(VI))}$ = 3.25) (Table 3; Fig. 7D). The behavior that has been observed may be explained by variations in the number, activity, and kinds of activated functioning receptors of U(VI) ions of DI and CD/ZD as temperature varies.[1,53] On the other hand, the temperature rise up to 308 K decreases the aggregation tendencies of the U(VI) ions prior to their interactions with the exteriors of DA and CD/ZD. With respect to ZD, the values obtained verify noticed escalation when the experimental temperature rises from 293 K ($n_{(U(VI))}$ = 3.06) until 313 K ($n_{(U(VI))}$ = 4.07) (Table 3; Fig. 7D). This was explained by the notable rise in U(VI) aggregation characteristics throughout the ZD exterior interface when uranium ions interacted with the zeolite framework at high temperatures.[30]

3.2.9.2 Occupied active sites density (N_m). The evaluation of the density of uranium-occupied sites ($N_{m\ (U(VI))}$) of DI, ZD, and CD/ZD provides insight into the total quantity of binding sites present on the surfaces of their particles during the course of the process. The $N_{m\ (U(VI))}$ values acquired for DI were 55.78 mg g^{-1} at 293 K, 49.8 mg g^{-1} at 308 K, and 33.7 mg g^{-1} at 313 K. The values demonstrated notable enhancement subsequent to the application of zeolitization transformations (ZD), yielding values of 85.73 mg g^{-1} (293 K), 59.8 mg g^{-1} (308 K), and

Table 3 The mathematical parameters of the studied advanced isotherm model

Steric and energetic parameters						
		n	N_m (mg g^{-1})	Q_{sat} (mg g^{-1})	$C_{1/2}$ (mg L^{-1})	ΔE (kJ mol^{-1})
DI	293 K	3.40	55.78	189.7	77.07	−4.55
	303 K	3.30	49.8	164.3	80.23	−4.6
	313 K	4.08	33.7	137.5	81.8	−4.71
ZD	293 K	3.06	85.73	262.33	80.17	−4.45
	303 K	3.63	59.8	217.0	76.53	−4.7
	313 K	4.07	43.32	176.3	77.49	−4.85
CD/ZD	293 K	3.26	91.25	297.47	74.65	−4.63
	303 K	3.39	76.74	260.14	80.18	−4.61
	313 K	3.25	66.42	215.86	80.76	−4.72

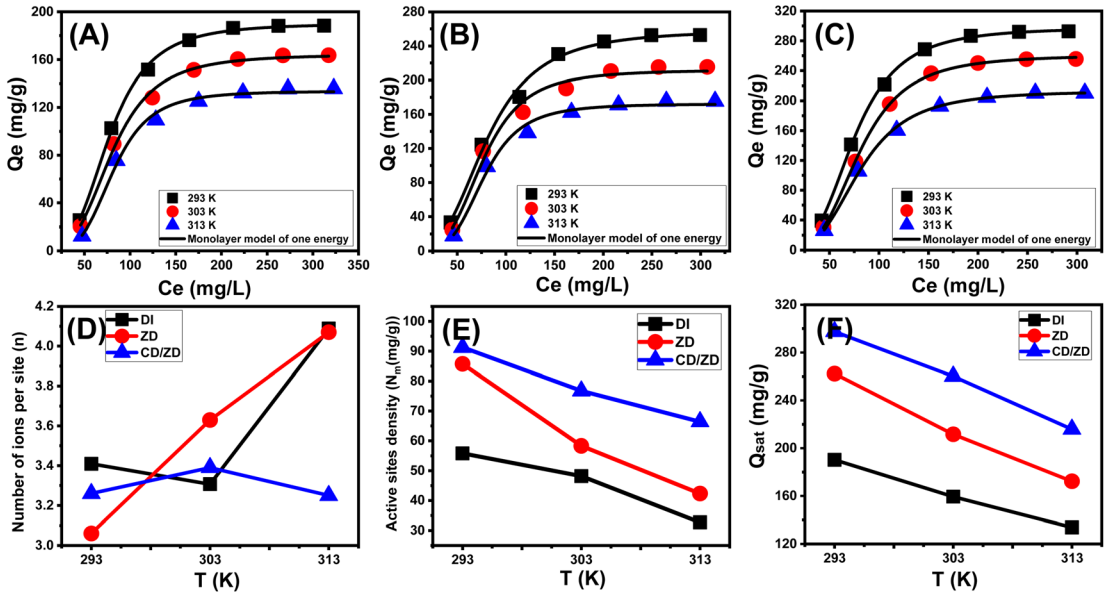

Fig. 7 Fitting of the U(VI) retention with advanced monolayer model of one energy site (DI (A), ZD (B), and CD/ZD (C)), changes in the number of adsorbed U(VI) ions per each active site (D), variations in the number of filled active sites throughout U(VI) retention (E), and changes in the U(VI) saturation adsorption capacities (F).

43.32 mg g^{-1} (313 K) (Fig. 7E; Table 3). Furthermore, subsequent to the incorporation of cyclodextrin (CD/ZD), there was a notable increase in the number of accessible active sites, resulting in values of 91.25 mg g^{-1} (293 K), 76.74 mg g^{-1} (308 K), and 66.42 mg g^{-1} (313 K) (Fig. 7E; Table 3). The findings revealed a notable elevation in the total number of free sites after the zeolitizing process, which may be related to the influence of the ionic exchange processes taking place within the crystalline framework of the zeolite that was formed. Additionally, the surface area's noticeable rise and the remarkable presence of extensive structural nano-pores provide supplementary interacting surfaces for U(VI) ions together with additional active sites. The improvements realized a significant boost subsequent to the hybridization approach of the ZD particulates with CD polymers. This phenomenon might be attributable to the addition of newly influential sites associated with the functional units of CD, with the established elevation of the surface area, hence facilitating a greater contact surface between the solution's U(VI) ions and composite. In relation to the impact of temperature, it can be observed that the density of filled active sites (N_m) by the uranium ions retained, along with their associated behaviours, exhibits an overall reduction as the evaluating temperature increases. This trend is evident in the case of DI as well as ZD and CD/ZD. This observation illustrates the adverse influence of high temperatures on the frequency of active sites as well as the deactivation of some effective sites that are already present, as well as the contact time required for efficient uranium ion retention by these sites. Previous research has shown that comparable behaviors were seen and attributed to the anticipated release of sequestered uranium ions from the outermost layer of silicate-based products. This release occurred as the saturation points of the heating solutions decreased due to effective adsorption activities.[54] The observed outcomes for both DI and ZD are in substantial agreement with the established values of $n_{(U(VI))}$ and the patterns of aggregation. The increase in the binding affinities of the uranium ions led to a discernible reduction in the quantity of filled sites.[55] The correlation between the $N_{m\ (U(VI))}$ and $n_{(U(VI))}$ values of CD/ZD in response to temperature was not seen, as both parameters exhibit similar trends with changes in temperature. The findings of this study indicate that the observed variations in the values of $n_{(U(VI))}$ can be primarily attributed to the aggregation characteristics and interionic interactions of the uranium ions. These factors have a more significant influence compared to the interaction between the uranium ions and the blended surface, as well as the presence and/or activation of the functional retention receptors with fluctuations in temperature.

3.2.9.3 Adsorption capacity at the saturation state of (Q_{sat}). The analysis of the U(VI) retaining characteristics of DI, ZD, and CD/ZD in a saturating state (Q_{sat}) has the potential to yield the most precise estimation of their maximal adsorption capacities. The results of Q_{sat} are heavily impacted by the determined densities of the filled sites ($N_{m\ (U(VI))}$) and the number of U(VI) ions accumulated at each site ($n_{(U(VI))}$). Diatomite, as an adsorbent for U(VI), has determined levels of Q_{sat} at 293 K to be 189.7 mg g^{-1}. At 308 K, the Q_{sat} level decreases to 164.3 mg g^{-1}, and at 313 K, it further decreases to 137.5 mg g^{-1} (Fig. 3F; Table 3). The zeolitized product (ZD) demonstrates improved retention qualities across various temperature conditions. At a temperature of 293 K, the adsorption capacity reaches a maximum value of 262.3 mg g^{-1}. The adsorption capacity at a temperature of 308 K has been determined to be 217 mg g^{-1}, whereas at a temperature of 313 K, it is found to be 176.3 mg g^{-1} (Fig. 3F; Table 3). The observed improvement underwent a significant rise subsequent to the creation of the composite (CD/ZD), leading to measurements of 297.4 mg g^{-1} (293 K),

260.1 mg g^{-1} (308 K), and 215.8 mg g^{-1} (313 K) (Fig. 3F; Table 3). The adverse effects of temperature ultimately led to the determination that DI, ZD, and CD/ZD demonstrate exothermic behaviour in their U(VI) adsorption capabilities. This demonstrated how the evaluation temperature accelerates the thermal collision properties associated with retention, lowering the efficacy of U(VI) binding. Moreover, the observed characteristics of Q_{sat} in relation to changes in temperature demonstrate a noteworthy accord with previously established properties of $N_{m\ (U(VI))}$ *vs.* $n_{(U(VI))}$. This implies that the effectiveness of U(VI) retention is mostly determined by the number of functional sites instead of the theoretical capacity of each active site for DI, ZD, and CD/ZD.

3.2.10 Adsorption energy. Determining the energy variations (ΔE) linked to the retention operations of U(VI) might provide important comprehension of the mechanics that underlie the processes, regardless of whether the effects are regulated by physical or chemical influences. Chemical paths usually have energies greater than 80 kJ mol^{-1}, whereas physical processes usually have energies less than 40 kJ mol^{-1}. Various kinds of physical mechanistic responses may be distinguished based on the measurement of adsorption energies. The mechanisms that are being highlighted include hydrophobic relationships (possess energy value of 5 kJ mol^{-1}), dipole–dipole forces (possess energy from 2 to 29 kJ mol^{-1}), coordination exchange (possess energy value of 40 kJ mol^{-1}), van der Waals attraction (possess energy from 4 to 10 kJ mol^{-1}), and hydrogen binding (possess energy less than 30 kJ mol^{-1}).[30,56] Eqn (5) was used to compute and determine the U(VI) retention energies (E), which include the measured solubility of U(VI) in examining the water-based solution (S), the value of the gas constant (R = 0.008314 kJ mol^{-1} K^{-1}), the U(VI) concentration during the half-saturated state of DI, ZD, and CD/ZD, alongside the absolute temperature (T).[55]

$$\Delta E = RT \ln\left(\frac{S}{C}\right) \quad (5)$$

The calculated removal energies of U(VI) by DI and ZD are between −4.5 and −4.77 kJ mol^{-1} and −4.4 and −4.8 kJ mol^{-1}, respectively. Meanwhile, the predicted CD/ZD values show a range of −4.6 to −4.7 kJ mol^{-1}. Therefore, physical processes including dipole–dipole forces (2 to 29 kJ mol^{-1}), the force of van der Waals (4 to 10 kJ mol^{-1}), and hydrogen binding (<30 kJ mol^{-1}) were the main causes of the retention of U(VI) by DI, ZD, and CD/ZD. Furthermore, the results of the experiments regarding the exothermic behavior of these operations are in accordance with the negative results of ΔE associated with the U(VI) capturing activities by DI, ZD, and CD/ZD.

3.2.11 Thermodynamic functions

3.2.11.1 Entropy. The entropy (S_a) associated with the uptake of U(VI) by DI, ZD, and CD/ZD provides insights into the particle's order and disorder qualities when exposed to various levels of U(VI) and temperature conditions. The S_a aspects have been emphasized by eqn (6) based on the earlier determined N_m and n values, as well as the U(VI) levels throughout the half-saturation phases of DI, ZD, and CD/ZD ($C_{1/2}$).[53]

$$\frac{S_a}{K_B} = N_m \left\{ \ln\left(1 + \left(\frac{C}{C_{1/2}}\right)^n\right) - n\left(\frac{C}{C_{1/2}}\right)^n \frac{\ln\left(\frac{C}{C_{1/2}}\right)}{1 + \left(\frac{C}{C_{1/2}}\right)^n} \right\} \quad (6)$$

The findings that have been obtained demonstrate a notable decrease in entropy levels (S_a) upon the uptake of U(VI) *via* DI, ZD, and CD/ZD, especially at elevated U(VI) concentrations. The data presented in Fig. 8A–C suggest a notable decline in the disordered attributes of interfaces of DI, ZD, and CD/ZD with increasing the tested levels of U(VI) ions. The examination of entropy properties in the aforementioned studies supports the hypothesis that U(VI) ions effectively dock onto the functioning active positions of DI, ZD, and CD/ZD, as well as vacant interaction receptors, when the concentration of U(VI) is relatively low.[55,57] During the process of retaining U(VI) by DI, it was observed that the greatest extent of entropy could be detected at equilibrium values of 75.1 mg L^{-1} (293 K), 82.12 mg L^{-1} (308 K), and 84.9 mg L^{-1} (313 K) (Fig. 8A). The equilibrium levels of greatest entropy, as evaluated for ZD, have been reported to be 75.1 mg g^{-1} at a temperature of 293 K, 76.6 mg g^{-1} at 308 K, and 80.2 mg g^{-1} at 313 K (Fig. 8B). The maximum entropy values observed during the application of CD/ZD are 71.7 mg L^{-1} (at a temperature of 293 K), 76.3 mg L^{-1} (at a temperature of 308 K), and 78.8 mg L^{-1} (at a temperature of 313 K) (Fig. 8C). The computed equilibrium concentrations exhibit a strong correlation with the anticipated U(VI) concentrations within the half-saturation situations for DI, ZD, and CD/ZD. As a result, the reactive binding sites become inaccessible for subsequent docking.

Furthermore, the empirical findings indicate a significant decrease in entropy values, indicating a decrease in the number of vacant sites as well as a noticeable decline in the attributes of freedom and mobility exhibited by the U(VI) ions.[58]

3.2.11.2 Internal energy and free enthalpy. The current work assesses the internal energy (E_{int}) corresponding to the retention processes of U(VI) by DI, ZD, and CD/ZD, considering the tested temperature and U(VI) concentration. Furthermore, this study investigates the impact of variability in the starting levels of U(VI) and the assessment temperature on the resulting changes of free enthalpy (G). The evaluation is performed based on the factors described in eqn (7) and (8), which rely on the predetermined values of N_m, n, and $C_{1/2}$, along with the translation partition (Z_v).[53,55]

$$\frac{E_{int}}{K_B T} = nN_m \left[\left(\frac{\left(\frac{C}{C_{1/2}}\right)^n \ln\left(\frac{C}{Z_v}\right)}{1 + \left(\frac{C}{C_{1/2}}\right)^n} \right) - \left(\frac{n \ln\left(\frac{C}{C_{1/2}}\right)\left(\frac{C}{C_{1/2}}\right)^n}{1 + \left(\frac{C}{C_{1/2}}\right)^n} \right) \right] \quad (7)$$

$$\frac{G}{K_B T} = nN_m \frac{\ln\left(\frac{C}{Z_v}\right)}{1 + \left(\frac{C_{1/2}}{C}\right)^n} \quad (8)$$

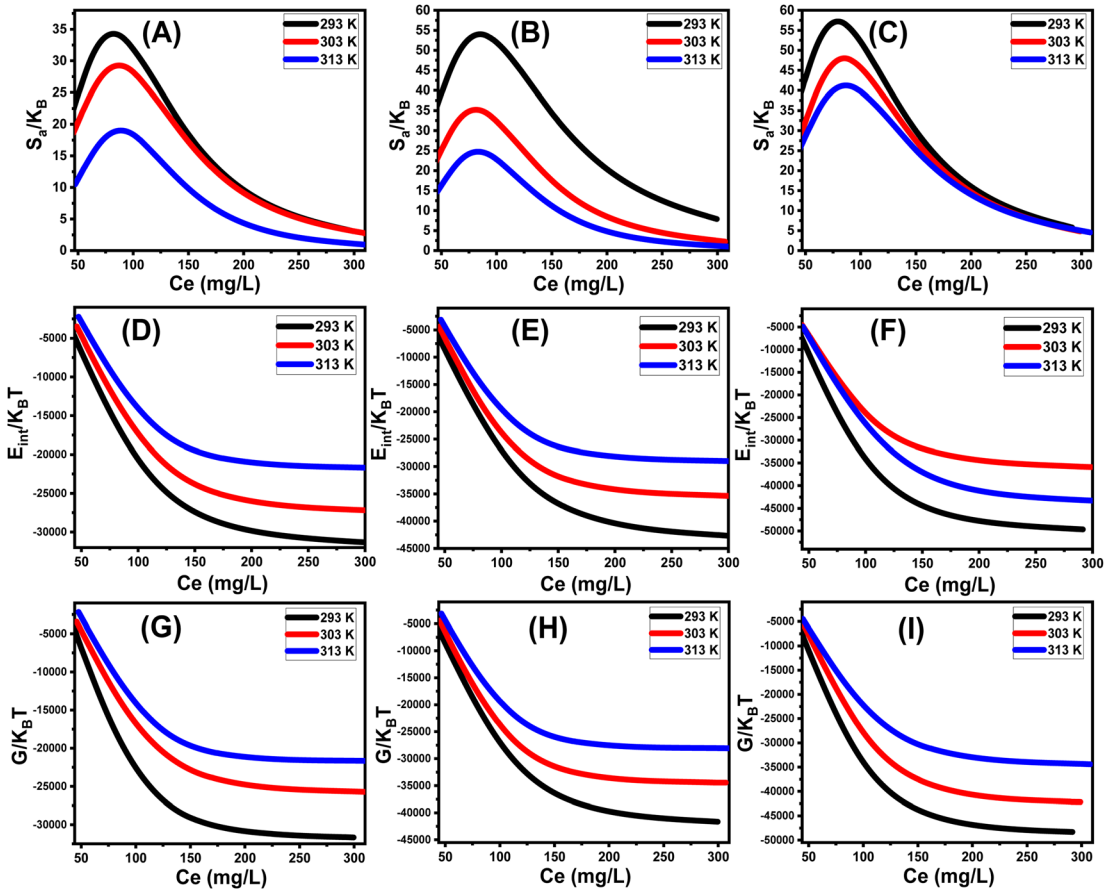

Fig. 8 The alteration in entropy characteristics when U(VI) ions are being retained (DI (A), ZD (B), and CD/ZD (C)), internal energy properties (DI (D), ZD (E), and CD/ZD (F)), and free enthalpy properties (DI (G), ZD (H), and CD/ZD (I)).

The calculated quantities of internal energies (E_{int}) during the adsorption processes of U(VI) onto DI, ZD, and CD/ZD demonstrate negative trends (Fig. 8D–F). The findings of the present investigation reveal a notable decrease in internal energy (E_{int}) when the operating temperature is raised from 293 K to 313 K (Fig. 8D–F). As a result, the sequestration pathways of DI, ZD, and CD/ZD for U(VI) exhibit greater levels of spontaneous behaviour and exothermicity. Comparable behaviours and characteristics have been noted for enthalpy levels that were established (Fig. 8G–I). The *G* levels show declining trends and have reversible relationships with the assessed temperature, indicating that the feasibility qualities are declining. This result strengthens the spontaneous and exothermic activity of U(VI)-retained reactions *via* DI, ZD, and CD/ZD.

3.2.12 Recyclability. To determine if synthetic ZD and CD/ZD are suitable for implementation in business-related and industrial-scale activities, reusable quality studies have been carried out. The ZD and CD/ZD particles were subjected to a washing protocol involving immersion in a diluted solution of NH_4Cl (1 mol L^{-1}) over a period of 10 minutes in order to facilitate their regeneration. The process had been assisted by employing a magnetic stirrer to enhance the elution efficiency and promote the release of the bound U(VI) ions. Following that, the particulates were separated *via* filtration and afterwards underwent an additional washing step utilizing distilled water over a period of 10 minutes. Following that, the particles underwent a drying process spanning 10 hours at a selected temperature of about 60 °C in preparation for their further use in a series of adsorption cycles. The experiment has been carried out by employing five repetitions to assess the removal potential of U(VI) ions. The experimental variables that were manipulated included the solid dosage (0.2 g L^{-1}), volume (200 mL), U(VI) concentration (350 mg L^{-1}), duration (a total of 24 hours), pH 5, and temperature (293 K).

The experimental results pertaining to the uptake effectiveness of U(VI) ions suggest that ZD and CD/ZD demonstrate a high level of stability, displaying significant prospects for recyclability. Regarding the reusing of ZD during its retention of U(VI) ions, the product demonstrated an uptake capability of more than 250 mg g^{-1} during two cycles, surpassing 234 mg g^{-1} during three cycles, and more than 210 mg g^{-1} across the course of five cycles (Fig. 9). For the recycling of CD/ZD, the eliminating capacities have been determined to go beyond 290 mg g^{-1} over the course of two cycles, beyond 281 mg g^{-1} across three cycles, and surpassing 254 mg g^{-1} across a total of five cycles. The decrease in the sequestration efficiency of U(VI) ions using ZD and CD/ZD products, as demonstrated through a linear fall, can be related to the continuous formation of complexes between

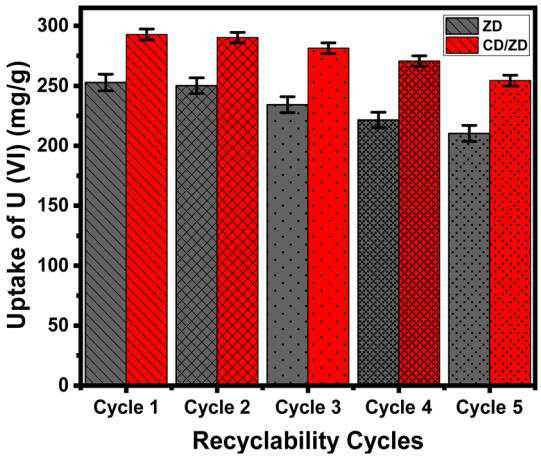

Fig. 9 Recyclability properties of ZD and CD/ZD during the retention of U(VI) ions.

the retained U(VI) ions and reactive binding sites that characterize the structures of ZD and CD/ZD. This behavior becomes more pronounced with a rise in the number of recycled and reused cycles. The formation of such complexes results in a reduction in the quantity of available and vacant binding sites during adsorption.

3.2.13 Suggested mechanism. The regulatory mechanisms involved in the retention of U(VI) *via* DI, ZD, and CD/ZD have been evaluated using advanced equilibrium analyses and the functional chemical elements that compose the structures, together with previously published literature. The examination of the energy levels associated with advanced equilibrium simulations reveals that U(VI) may potentially be retained on the surfaces of DI, ZD, and CD/ZD by dipole–dipole forces (2 to 29 kJ mol^{-1}), van der Waals forces (4 to 10 kJ mol^{-1}), and hydrogen bonding (<30 kJ mol^{-1}). Furthermore, the incorporation of U(VI) into the siliceous surface of DI may also occur *via* electrostatic attractions together with chemical-based complexation involving the U(VI) ions and the active silanol groups existing across DI. The zeolite phase may retain U(VI) *via* additional mechanisms such as ion exchange and conventional adsorption events.[49] The operation of the ion exchange mechanism involves the substitution of both structurally and loosely bound zeolitic ions with U(VI).[50] The subsequent stage is characterized by the prevalence of interior complexation or the adsorption process, which entails the establishment of chemical bindings involving U(VI) ions together with the main functional groups of zeolite, in addition to high electrostatic attractions along with coulombic attracting forces.[51] Following the functioning procedure, the aforementioned mechanisms are further strengthened by the electrostatic characteristics of the newly incorporated chemical groups of the CD polymer. Additionally, the carboxylic groups of the polymeric chains serve as the foundational centers for the development of complexes with U(VI).[52]

3.2.14 Comparison study. The determined retention results for U(VI) using DI, ZD, and CD/ZD were compared with the other reported adsorbents in the literature. As demonstrated in Table 4, the finally obtained composite CD/ZD displays higher efficiency than raw diatomite and zeolitized diatomite, and most of the presented adsorbents in the table, including some metal oxides, either in composite or pure phases. This demonstrates the value of the synthetic composite as a low-cost, safe, and highly effective adsorbent that qualifies for realistic remediation applications of U(VI) ions.

Table 4 Comparison between the retention capacities of the studied structures and other materials in literature

Adsorbent	$Q_{(max)}$ (mg g^{-1})	Reference
Amidoxime chitosan/bentonite	49.09	53
Fe_3O_4	125	54
SBA-15	208	55
Polyacrylamide/chelating sorbents	65.3	56
MCM-48	125	57
nZVI/CNF	54.95	58
Nickel ferrite/graphene oxide	123	59
Montmorillonite–Fe_3O_4–TiO_2	109.11	60
Activated carbon	158	61
Graphene oxide nanosheets	97.5	62
Fe_3O_4@TiO_2	118.8	63
Carbonaceous nanofibers	125	64
Fe_3O_4@C	120.2	65
$MnFe_2O_4$	119.9	66
GO–MnO_2	85.2	67
DI	**189.7**	**This study**
ZD	**262.3**	**This study**
CD/ZD	**297.5**	**This study**

4 Conclusions

The diatomite's silica-containing frustules were effectively transformed into synthesized zeolite (ZD) and subsequently modified with β-cyclodextrin (CD/ZD) to boost their adsorption potential for U(VI). The blending of CD and ZD (CD/ZD) resulted in enhanced retention capacity (297.5 mg g^{-1}), in contrast to both ZD (262.3 mg g^{-1}) and DI (189.7 mg g^{-1}). This reflects the impact of the hybridization process in inducing the surface area, ion exchange properties, quantities of receptor sites, and surficial reactivity of the obtained CD/ZD composite. This was corroborated by the analyzed density of binding sites as a steric factor (91.2 mg g^{-1} (CD/ZD), 85.7 mg g^{-1} (ZD), and 55.7 mg g^{-1} (DI)). The obtained energetic results reveal the controlling effect of the physical mechanisms (van der Waals forces, dipole forces, and ion exchange reactions) during the retention of U(VI) either by ZD or CD/ZD. The exothermicity and spontaneity behaviors of the retention reactions of U(VI) by CD/ZD were concluded based on the assessed entropy, internal energy, and free enthalpy aspects.

Conflicts of interest

There are no conflicts to declare.

Acknowledgements

This work was supported and funded by the Deanship of Scientific Research at Imam Mohammad Ibn Saud Islamic University (IMSIU) (grant number IMSIU-RP23048).

References

1 S. Asghar, M. Roudgar-Amoli, A. Alizadeh and Z. Shariatinia, Water Purification Through Adsorption of Organic Pollutant onto Novel and Effective Phosphorus-Containing g-C_3N_4/$FeMo_{0.5}O_3$ Nanocomposites, *Water, Air, Soil Pollut.*, 2023, **234**(1), 43.

2 A. Raj, R. M. Rego, K. V. Ajeya, H. Y. Jung and M. D. Kurkuri, Basil seeds loaded with MOFs as an eco-friendly and sustainable adsorbent for efficient removal of hazardous organic pollutants from water, *Sep. Purif. Technol.*, 2024, **330**, 125370.

3 J. Yuan, C. Wang, Z. Tang, T. Chu, C. Zheng, Q. Han, H. Chen and Y. Tan, Biochar derived from traditional Chinese medicine residues: An efficient adsorbent for heavy metal Pb (II), *Arabian J. Chem.*, 2024, 105606.

4 W. Li, M. Guo, Y. Wang, H. Deng, H. Lei, C. Yu and Z. Liu, Selective adsorption of heavy metal ions by different composite-modified semi-carbonized fibers, *Sep. Purif. Technol.*, 2024, **328**, 125022.

5 F. Javaheri, Z. Kheshti, S. Ghasemi and A. Altaee, Enhancement of Cd^{2+} removal from aqueous solution by multifunctional mesoporous silica: Equilibrium isotherms and kinetics study, *Sep. Purif. Technol.*, 2019, **224**, 199–208.

6 M. A. Salam, M. R. Abukhadra and M. Mostafa, Effective decontamination of As (V), Hg (II), and U (VI) toxic ions from water using novel muscovite/zeolite aluminosilicate composite: adsorption behavior and mechanism, *Environ. Sci. Pollut. Res.*, 2020, **27**(12), 13247–13260.

7 S. J. Park, S. S. Shin, J. H. Jo, C. H. Jung, H. Park, Y. I. Park, H. J. Kim and J. H. Lee, Tannic acid-assisted in-situ interfacial formation of Prussian blue-assembled adsorptive membranes for radioactive cesium removal, *J. Hazard. Mater.*, 2023, **442**, 129967.

8 S. Kang, J. Lee, S. M. Park, D. S. Alessi and K. Baek, Adsorption characteristics of cesium onto calcium-silicate-hydrate in concrete powder and block, *Chemosphere*, 2020, **259**, 127494.

9 Z. Lv, H. Wang, C. Chen, S. Yang, L. Chen, A. Alsaedi and T. Hayat, Enhanced removal of uranium (VI) from aqueous solution by a novel Mg-MOF-74-derived porous MgO/carbon adsorbent, *J. Colloid Interface Sci.*, 2019, **537**, A1–A10.

10 W. Mu, S. Du, X. Li, Q. Yu, R. Hu, H. Wei, Y. Yang and S. Peng, Efficient and irreversible capture of strontium ions from aqueous solution using metal–organic frameworks with ion trapping groups, *Dalton Trans.*, 2019, **48**(10), 3284–3290.

11 F. Zahran, H. H. El-Maghrabi, G. Hussein and S. M. Abdelmaged, Fabrication of bentonite based nanocomposite as a novel low cost adsorbent for uranium ion removal, *Environ. Nanotechnol., Monit. Manage.*, 2019, **11**, 100205.

12 Z. Lu, J. Yu, H. Zeng and Q. Liu, Polyamine-modified magnetic graphene oxide nanocomposite for enhanced selenium removal, *Sep. Purif. Technol.*, 2017, **183**, 249–257.

13 M. Dittmar, Nuclear energy: Status and future limitations, *Energy*, 2012, **37**(1), 35–40.

14 J. Song, B. Han, H. Song, J. Yang, L. Zhang, P. Ning and Z. Lin, Nonreductive biomineralization of uranium by Bacillus subtilis ATCC-6633 under aerobic conditions, *J. Environ. Radioact.*, 2019, **208**, 106027.

15 X. L. Wang, Y. Li, J. Huang, Y. Z. Zhou, B. L. Li and D. B. Liu, Efficiency and mechanism of adsorption of low concentration uranium in water by extracellular polymeric substances, *J. Environ. Radioact.*, 2019, **197**, 81–89.

16 J. Park, J. Bae, K. Jin and J. Park, Carboxylate-functionalized organic nanocrystals for high-capacity uranium sorbents, *J. Hazard. Mater.*, 2019, **371**, 243–252.

17 S. Kwon, Y. Kim and Y. Roh, Cesium removal using acid- and base-activated biotite and illite, *J. Hazard. Mater.*, 2021, **401**, 123319.

18 A. Kausar, S. T. Zohra, S. Ijaz, M. Iqbal, J. Iqbal, I. Bibi, S. Nouren, N. El Messaoudi and A. Nazir, Cellulose-based materials and their adsorptive removal efficiency for dyes: A review, *Int. J. Biol. Macromol.*, 2023, **224**, 1337–1355.

19 G. S. dos Reis, G. L. Dotto, J. Vieillard, M. L. Oliveira, S. F. Lütke, L. F. Silva, E. C. Lima, N. P. Salau and U. Lassi, Uptake the rare earth elements Nd, Ce, and La by a commercial diatomite: kinetics, equilibrium, thermodynamic and adsorption mechanism, *J. Mol. Liq.*, 2023, **389**, 122862.

20 J. Wang, G. Zhang, S. Qiao and J. Zhou, Comparative assessment of formation pathways and adsorption behavior reveals the role of NaOH of MgO-modified diatomite on phosphate recovery, *Sci. Total Environ.*, 2023, **876**, 162785.

21 H. B. Fan, Q. F. Ren, S. L. Wang, Z. Jin and Y. Ding, Synthesis of the Ag/Ag_3PO_4/diatomite composites and their enhanced photocatalytic activity driven by visible light, *J. Alloys Compd.*, 2019, **775**, 845–852.

22 T. P. P. Coelho, B. P. Bezerra, J. R. Verza, A. P. Luz and M. R. Morelli, Physico-mechanical properties of metakaolin and diatomite-based geopolymers, *Mater. Lett.*, 2023, **349**, 134784.

23 C. Tramontano, B. Miranda, G. Chianese, L. De Stefano, C. Forestiere, M. Pirozzi and I. Rea, Design of gelatin-capped plasmonic-diatomite nanoparticles with enhanced galunisertib loading capacity for drug delivery applications, *Int. J. Mol. Sci.*, 2021, **22**(19), 10755.

24 F. Zobi, Diatom biosilica in targeted drug delivery and biosensing applications: Recent studies, *Micro*, 2022, **2**, 342–360.

25 Z. Zhang, Z. Zou, X. Ren, Y. Huang, Y. Deng and H. Zheng, Preparation and Optimization of the Adsorbent for Phosphorus Removal Using the Response Surface Method, *Magnetochemistry*, 2024, **10**(1), 5.

26 F. Shajarat, K. Ghanemi, M. Alimoradi and M. Ramezani, Nanostructured composite of polydopamine/diatomite-based biosilica to enhance the extraction of phthalate esters from aqueous samples, *Microchem. J.*, 2022, **174**, 107060.

27 F. Baba, F. Benaliouche, R. Meknaci and Y. Boucheffa, Water adsorption and antibacterial activity studies for characterization of Ca-LTA zeolite/diatomite adsorbents, *Colloid Interface Sci. Commun.*, 2020, **35**, 100233.

28 J. M. Moreno-Maroto, J. Alonso-Azcárate, C. Martínez-García, M. Romero, A. López-Delgado and T. Cotes-Palomino, Zeolitization of Diatomite Residues by a Simple Method, *Appl. Sci.*, 2022, **12**(21), 10977.

29 L. Sun, J. Wu, J. Wang, G. Yu, J. Liu, Y. Du, Y. Li and H. Li, Controlled synthesis of Zeolite adsorbent from low-grade diatomite: A case study of self-assembled sodalite microspheres, *J. Environ. Sci.*, 2020, **91**, 92–104.

30 J. Jia, D. Wu, J. Yu, T. Gao, L. Guo and F. Li, Upgraded β-cyclodextrin-based broad-spectrum adsorbents with enhanced antibacterial property for high-efficient dyeing wastewater remediation, *J. Hazard. Mater.*, 2024, **461**, 132610.

31 N. Altoom, S. M. Ibrahim, S. I. Othman, A. A. Allam, H. A. Alqhtani, F. S. Al-Otaibi and M. R. Abukhadra, Characterization of β-cyclodextrin/phillipsite (β-CD/Ph) composite as a potential carrier for oxaliplatin as therapy for colorectal cancer; loading, release, and cytotoxicity, *Colloids Surf., A*, 2022, **648**, 129144.

32 B. F. Dizaji, M. H. Azerbaijan, N. Sheisi, P. Goleij, T. Mirmajidi, F. Chogan, M. Irani and F. Sharafian, Synthesis of PLGA/chitosan/zeolites and PLGA/chitosan/metal organic frameworks nanofibers for targeted delivery of Paclitaxel toward prostate cancer cells death, *Int. J. Biol. Macromol.*, 2020, **164**, 1461–1474.

33 M. Servatan, P. Zarrintaj, G. Mahmodi, S. J. Kim, M. R. Ganjali, M. R. Saeb and M. Mozafari, Zeolites in drug delivery: Progress, challenges and opportunities, *Drug Discovery Today*, 2020, **25**, 642–656.

34 A. M. El-Sherbeeny, S. M. Ibrahim, A. A. AlHammadi, A. T. A. Soliman, J. J. Shim and M. R. Abukhadra, Effective retention of radioactive Cs^{+} and Ba^{2+} ions using β-cyclodextrin functionalized diatomite (β-CD/D) as environmental adsorbent; characterization, application, and safety, *Surf. Interfaces*, 2021, **26**, 101434.

35 S. Sadjadi and F. Koohestani, Composite of β-cyclodextrin and bentonite clay: a promising support for Pd immobilization and developing a catalyst for hydrogenation of nitroarenes under mild reaction condition, *J. Phys. Chem. Solids*, 2021, **151**, 109894.

36 K. Krawczyk, D. Silvestri, N. H. Nguyen, A. Ševců, D. Łukowiec, V. V. Padil, M. Řezanka, M. Černík, D. D. Dionysiou and S. Wacławek, Enhanced degradation of sulfamethoxazole by a modified nano zero-valent iron with a β-cyclodextrin polymer: Mechanism and toxicity evaluation, *Sci. Total Environ.*, 2022, **817**, 152888.

37 M. Khatamian, N. Afshar, S. Hosseini Nami and S. Fazli-Shokouhi, Synthesis and characterization of zeolite A, Fe_3O_4/zeolite A, and Fe_2O_3/zeolite A nanocomposites and investigation of their arsenic removal performance, *J. Iran. Chem. Soc.*, 2023, **20**(7), 1657–1670.

38 J. Jia, D. Wu, J. Yu, T. Gao, J. Li, L. Guo and F. Li, β-cyclodextrin-based adsorbents integrated with N-doped TiO_2 photocatalysts for boosting dye elimination of industrial wastewater, *Surf. Interfaces*, 2014, 103901.

39 Y. Jiang, M. R. Abukhadra, N. M. Refay, M. F. Sharaf, M. A. El-Meligy and E. M. Awwad, Synthesis of chitosan/MCM-48 and β-cyclodextrin/MCM-48 composites as bio-adsorbents for environmental removal of Cd^{2+} ions; kinetic and equilibrium studies, *React. Funct. Polym.*, 2020, **154**, 104675.

40 E. L. Vivas and K. Cho, Efficient adsorptive removal of cobalt (II) ions from water by dicalcium phosphate dihydrate, *J. Environ. Manage.*, 2021, **283**, 111990.

41 K. Mishima, X. Du, N. Miyamoto, N. Kano and H. Imaizumi, Experimental and theoretical studies on the adsorption mechanisms of uranium (VI) ions on chitosan, *J. Funct. Biomater.*, 2018, **9**(3), 49.

42 Z. Xiao-teng, J. Dong-mei, X. Yi-qun, C. Jun-chang, H. Shuai and X. Liang-shu, Adsorption of uranium (VI) from aqueous solution by modified rice stem, *J. Chem.*, 2019, DOI: **10.1155/2019/6409504**.

43 E. El Qada, Kinetic Behavior of the Adsorption of Malachite Green Using Jordanian Diatomite as Adsorbent, *Jordanian J. Eng. Chem. Ind.*, 2020, **3**(1), 1–10.

44 X. Lin, Y. Xie, H. Lu, Y. Xin, R. Altaf, S. Zhu and D. Liu, Facile preparation of dual La-Zr modified magnetite adsorbents for efficient and selective phosphorus recovery, *Chem. Eng. J.*, 2021, **413**, 127530.

45 Y. A. B. Neolaka, Y. Lawa, J. Naat, A. C. Lalang, B. A. Widyaningrum, G. F. Ngasu, K. A. Niga, H. Darmokoesoemo, M. Iqbal and H. S. Kusuma, Adsorption of methyl red from aqueous solution using Bali cow bones (Bos javanicus domesticus) hydrochar powder, *Results Eng.*, 2023, **17**, 100824.

46 A. Sherlala, A. Raman, M. M. Bello and A. Buthiyappan, Adsorption of arsenic using chitosan magnetic graphene oxide nanocomposite, *J. Environ. Manage.*, 2019, **246**, 547–556.

47 Y. Huang, X. Zeng, L. Guo, J. Lan, L. Zhang and D. Cao, Heavy metal ion removal of wastewater by zeolite-imidazolate frameworks, *Sep. Purif. Technol.*, 2018, **194**, 462–469.

48 E. E. Jasper, V. O. Ajibola and J. C. Onwuka, Nonlinear regression analysis of the sorption of crystal violet and methylene blue from aqueous solutions onto an agro-waste derived activated carbon, *Appl. Water Sci.*, 2020, **10**, 132.

49 K. Gedik and I. Imamoglu, Removal of cadmium from aqueous solutions using clinoptilolite: influence of pretreatment and regeneration, *J. Hazard. Mater.*, 2008, **155**, 385–392.

50 A. Benhammou, A. Yaacoubi, L. Nibou and B. Tanouti, Adsorption of metal ions onto Moroccan stevensite: kinetic and isotherm studies, *J. Colloid Interface Sci.*, 2005, **282**(2), 320–326.

51 N. Morali, Investigation of zinc and lead removal from aqueous solution using clinoptilolite, Published master's thesis, Middle East Technical University, Turkey, 2006.
52 X. L. Wang, Y. Li, J. Huang, Y. Z. Zhou, B. L. Li and D. B. Liu, Efficiency and mechanism of adsorption of low concentration uranium in water by extracellular polymeric substances, *J. Environ. Radioact.*, 2019, **197**, 81–89.
53 T. S. Anirudhan, G. S. Lekshmi and F. Shainy, Synthesis and characterization of amidoxime modified chitosan/bentonite composite for the adsorptive removal and recovery of uranium from seawater, *J. Colloid Interface Sci.*, 2019, **534**, 248–261.
54 L. Tan, J. Wang, Q. Liu, Y. Sun, H. Zhang, Y. Wang, X. Jing, J. Liu and D. Song, Facile preparation of oxine functionalized magnetic Fe_3O_4 particles for enhanced uranium (VI) adsorption, *Colloids Surf., A*, 2015, **466**, 85–91.
55 X. Wang, G. Zhu and F. Guo, Removal of uranium (VI) ion from aqueous solution by SBA-15, *Ann. Nucl. Energy*, 2013, **56**, 151–157.
56 A. A. Younes, A. M. Masoud and M. H. Taha, Amino-functionalised cross-linked polyacrylamide for the adsorption of U (VI) ions from contaminated aqueous solutions, *Int. J. Environ. Anal. Chem.*, 2023, **103**(20), 9117–9130.
57 K. Vidya, N. M. Gupta and P. Selvam, Influence of pH on the sorption behaviour of uranyl ions in mesoporous MCM-41 and MCM-48 molecular sieves, *Mater. Res. Bull.*, 2004, **39**, 2035e2048.
58 B. Hu, X. Mei, X. Li, J. Hu and D. Xu, Decontamination of U(VI) from n ZVI/CNF composites investigated by batch, spectroscopic and modeling techniques, *J. Mol. Liq.*, 2018, **237**, 1–9.
59 L. P. Lingamdinne, Y. L. Choi, I. S. Kim, J. K. Yang, J. R. Koduru and Y. Y. Chang, Preparation and characterization of porous reduced graphene oxide based inverse spinel nickel ferrite nanocomposite for adsorption removal of radionuclides, *J. Hazard. Mater.*, 2017, **326**, 145–156.
60 L. Bian, J. Nie, X. Jiang, M. Song, F. Dong, W. Li, L. Shang, H. Deng, H. He, B. Xu, B. Wang and X. Gu, Selective removal of uranyl from aqueous solutions containinga mix of toxic metal ions using Core-Shell MFe_2O_4-TiO_2 nanoparticles of montmorillonite edge sites, *ACS Sustain. Chem. Eng.*, 2018, **6**, 16267–16278.
61 A. Belgacem, R. Rebiai, H. Hadoun, S. Khemaissia and M. Belmedani, The removal of uranium (VI) from aqueous solutions onto activated carbon developed from grinded used tire, *Environ. Sci. Pollut. Res.*, 2014, **21**, 684e694.
62 G. Zao, T. Wen, X. Yang, S. Yang, J. Liao, J. Hu, D. Shao and X. Wang, Preconcentration of U(VI) ions on few-layered grapheme oxide nanosheets from aqueous solutions, *Dalton Trans.*, 2012, **41**, 6182–6188.
63 L. Tan, X. Zhang, Q. Liu, X. Jing, J. Liu, D. Song, S. Hu, L. Liu and J. Wang, Synthesis of Fe_3O_4@TiO_2 core–shell magnetic composites for highly efficient sorption of uranium (VI), *Colloids Surf., A*, 2015, **469**, 279–286.
64 Y. Sun, Z. Y. Wu, X. Wang, C. Ding, W. Cheng, S. H. Yu and Z. Wang, Macroscopic and microscopic investigation of U(VI) and Eu(III) adsorption on bacterium-derived carbon nanofibers, *Environ. Sci. Technol.*, 2016, **50**, 4459.
65 X. Zhang and J. Wang, Preparation of carbon coated Fe_3O_4 nanoparticles for magnetic separation of uranium, *Solid State Sci.*, 2018, **75**, 14–20.
66 Y. Hu, C. Zhao, L. Yin, T. Wen, Y. Yang, Y. Ai and X. Wang, Combining batch technique with theoretical calculation studies to analyze the highly efficient enrichment of U(VI) and Eu(III) on magnetic $MnFe_2O_4$ nanocubes, *Chem. Eng. J.*, 2018, **349**, 347–357.
67 N. Pan, L. Li, J. Ding, S. Li, R. Wang, Y. Jin, X. Wang and C. Xia, Preparation of graphene oxide-manganese dioxide for highly efficient adsorption and separation of Th (IV)/U (VI), *J. Hazard. Mater.*, 2016, **309**, 107–115.